

FIG. 2. (a) Lead-lag correlation coefficients (CCs) of the monthly Niño-3.4 index with the monthly PNA index. Composite monthly evolution of Niño-3.4 (black line) and PNA (yellow line) indices for (b) El Niño years and (c) La Niña years. The abscissa indicates 14 months from May of year(0) to June of year(1).

2. Data, methodology, and experimental designs

a. Data and methodology

Monthly 500-hPa geopotential height and horizontal wind data with a horizontal resolution of $2.5^{\circ} \times 2.5^{\circ}$ are obtained from the National Centers for Environmental Prediction/National Center for Atmospheric Research (NCEP/NCAR) Reanalysis (Kalnay et al. 1996). The monthly SST data on a $1^{\circ} \times 1^{\circ}$ grid are provided by the Met Office Hadley Centre (Rayner et al. 2003). Our analyses cover the period of 1979–2019, and anomalies for all variables are derived relative to the monthly mean climatology for the entire study period.

Based on the Climate Prediction Center definition, the PNA index is defined as a linear combination of area-averaged 500-hPa geopotential height anomalies over four centers of the PNA pattern, as follows:

PNA =
$$Z^*(15^\circ-25^\circ\text{N}, 180^\circ-140^\circ\text{W})$$

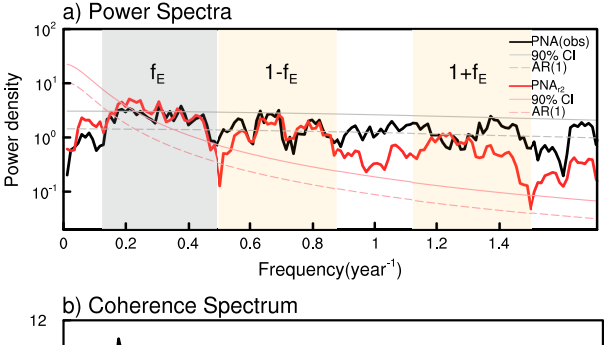
- $Z^*(40^\circ-50^\circ\text{N}, 180^\circ-140^\circ\text{W})$
+ $Z^*(45^\circ-60^\circ\text{N}, 125^\circ-105^\circ\text{W})$
- $Z^*(25^\circ-35^\circ\text{N}, 90^\circ-70^\circ\text{W})$,

where Z^* denotes the standardized 500-hPa geopotential height anomaly. We use the Niño-3.4 index (SST anomalies averaged over 5°S-5°N, 120°-170°W) as a measure of ENSO

intensity. Thirteen El Niño and twelve La Niña events (Table 1) are identified based on a threshold of $\pm 0.5^{\circ}$ C of the Niño-3.4 SST anomalies for five consecutive overlapping seasons, according to the definition of the Climate Prediction Center. ENSO years are labeled year(0)/year(1), where 0 and 1 refer to the ENSO developing and decaying years, respectively. The multitaper method (MTM) is used for spectral analysis with three tapers (Thomson 1982). All statistical significance tests are performed based on the two-tailed Student's t test. The effective number of degrees of freedom ($N_{\rm eff} = N/T$) is calculated to remove the influence of autocorrelation on the correlation significance (Davis 1976), where N denotes the sample size and $T = \sum_{j=-\infty}^{\infty} R_{xx}(j)R_{yy}(j)$, where $R_{xx}(j)$ and $R_{yy}(j)$ are the autocorrelation of two sample series at the lag time of j.

b. Experimental design

To test the impact of the seasonal modulation of ENSO on the PNA variability, two sets of numerical experiments are conducted with the Geophysical Fluid Dynamics Laboratory (GFDL) Atmospheric Model, version 2.1 (AM2.1), with a horizontal resolution of 2.5° × 2.5° (Anderson et al. 2004). In the first set of experiments (EXP1), the observed SST anomalies are imposed on the climatological annual cycle of SSTs in the tropical Pacific region (30°S–30°N, 110°E–90°W). The second set of experiments (EXP2) has the same SST anomaly forcing, but the climatological SSTs in the tropical Pacific are



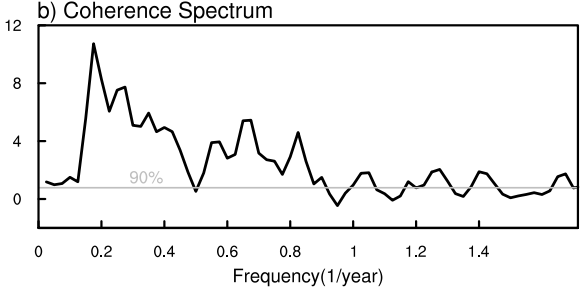
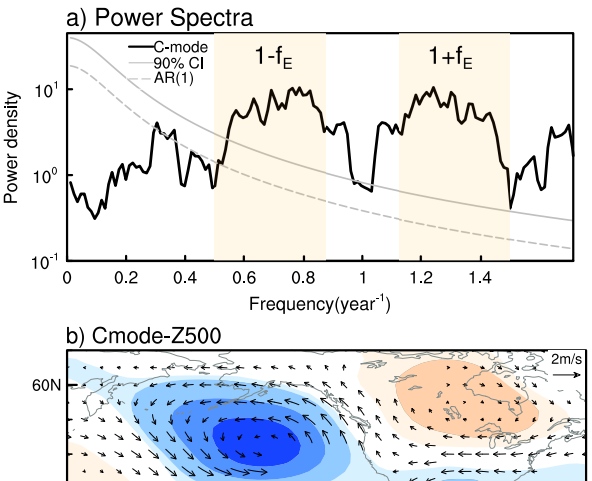


FIG. 3. (a) MTM power spectra of the observed PNA index (black thick line) and reconstructed PNA index using both the Niño-3.4 and C-mode indices (red thick line). Gray and red solid lines indicate their respective 90% confidence levels to autoregressive lag-1 [AR(1)] null hypotheses (gray and red dashed lines). The gray-shaded area indicates the ENSO dominant frequency band (f_E). The left and right yellow-shaded areas represent the frequency bands of $1-f_E$ and $1+f_E$, respectively. (b) Coherence spectrum between the observed PNA index and reconstructed PNA index using both the Niño-3.4 and C-mode indices. The solid line denotes the 90% confidence level.

specified as the September equinox conditions when the sun is located directly over the equator. The EXP2 experiment is designed to investigate the importance of the background SST annual cycle to the seasonal characteristics of the PNA teleconnection during ENSO years through intercomparison with the results of the EXP1. Each of these two sets of experiments consists of an ensemble of 10 simulations with perturbed initial conditions, which are integrated from January 1979 to December 2019. The ensemble mean is used to remove the possible influence of internal atmospheric variability.

3. Seasonal preference of the observed PNA response to ENSO

To better understand the relationship between ENSO and the PNA teleconnection, we first show the regressed 500-hPa geopotential height anomalies on the monthly PNA and Niño-3.4 indices, respectively (Figs. 1a,b). Figure 1a shows the typical PNA spatial structure, characterized by four wavelike action centers arching from the tropical Pacific across North America. The ENSO-associated geopotential height anomalies are, as expected, highly similar to the PNA spatial pattern (Fig. 1b), with a pattern correlation of 0.86. This supports the notion that ENSO-associated SST anomalies in the tropical Pacific can trigger the PNA teleconnection via shifts in



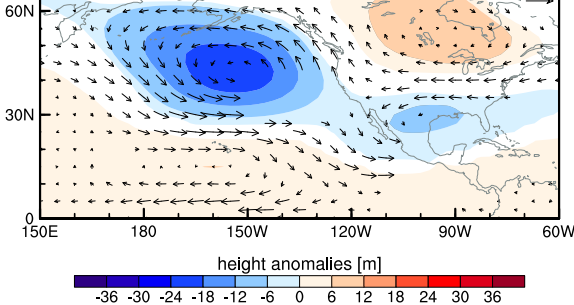


FIG. 4. (a) MTM power spectrum for the C-mode index (black line). The gray solid line denotes the 90% confidence level and the gray dashed line corresponds to the AR(1) null hypothesis. (b) 500-hPa geopotential height (shading; m) and horizontal wind (vectors; m s⁻¹) regressed upon the normalized monthly C-mode index. Shading represents height anomalies that are statistically significant at the 90% confidence level. The wind anomalies are shown only when they are significant at the 90% confidence level.

tropical convection, as established in many previous studies (e.g., Trenberth et al. 1998; Hoskins and Karoly 1981; Horel and Wallace 1981). Figure 1c shows the time evolution of the monthly Niño-3.4 and PNA indices with a 3-month running-mean filter applied to remove high-frequency noise from the PNA index. The monthly Niño-3.4 index is positively correlated with the monthly PNA index (R=0.45, statistically significant at the 99% confidence level), indicating that El Niño years usually correspond to a positive PNA index and La Niña years to a negative PNA index.

Of particular interest is that the peak of the PNA index tends to lag the peak of the Niño-3.4 index by about 2 months during ENSO years (Fig. 1c). It is evidenced by their lead–lag relationship, showing that the maximum positive correlation (R=0.54) occurs when the Niño-3.4 index leads the PNA index by 2 months (Fig. 2a). It should be noted that the ENSO and PNA linkage cannot be simply described as the relationship of a 2-month phase shift, since the time-evolution structure of the PNA teleconnection pattern is distinctively different from that of the ENSO SST. As shown in Figs. 2b and 2c, the Niño-3.4 SST anomalies during both ENSO warm and cold phases are typically characterized by a slow evolution from developing to decaying summers with the peak being in December. In contrast, the PNA teleconnection pattern exhibits a relatively sharp temporal behavior, rapidly intensifying

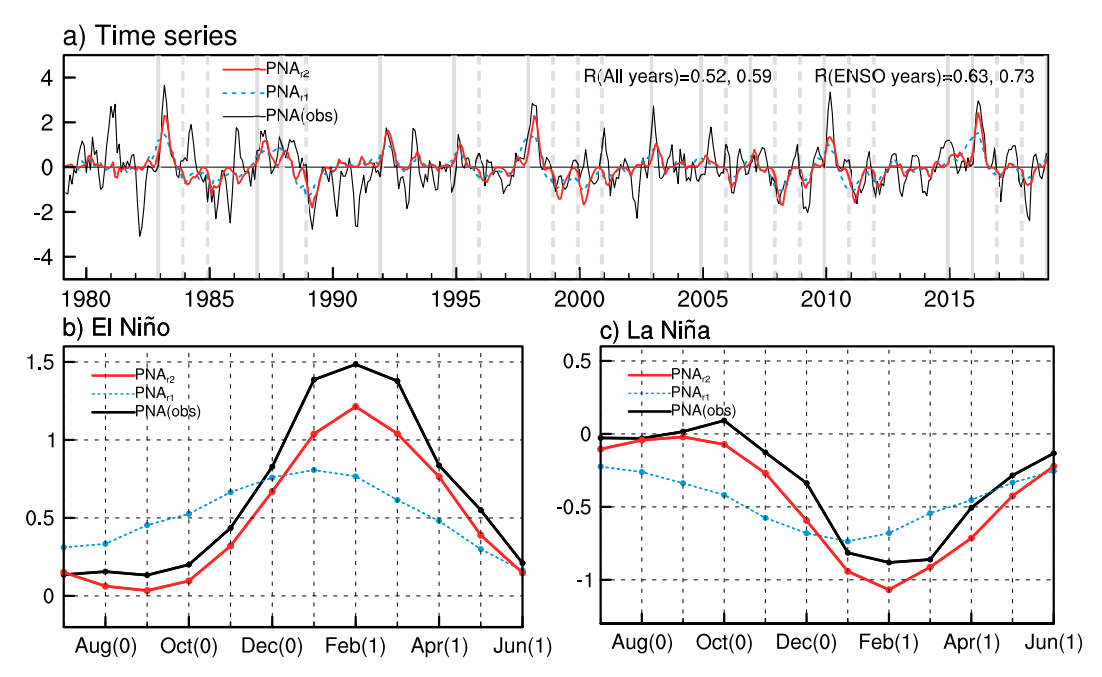


FIG. 5. (a) Time series of the observed PNA index [PNA(obs); black solid line], the PNA $_{r1}$ (blue dashed line), and the PNA $_{r2}$ (red solid line). The correlation coefficients of the PNA $_{r1}$ with the observed PNA indices during all years and during ENSO years only are 0.52 and 0.63, respectively. The correlation coefficients of the PNA $_{r2}$ with the observed PNA indices during all years and during ENSO years only are 0.59 and 0.73, respectively. The gray solid and dashed vertical gray lines correspond to El Niño and La Niña years, respectively. Composite monthly evolution of the PNA(obs) (black solid line), PNA $_{r1}$ (blue dashed line), and PNA $_{r2}$ (red solid line) for (b) El Niño years and (c) La Niña years. The abscissa indicates 12 months from July of year(0) to June of year(1).

from November, reaching its peak in February, and decaying after May.

4. Role of the ENSO combination mode in the PNA temporal evolution

To understand the characteristics of the PNA teleconnection temporal evolution, we next apply an MTM spectral analysis to examine the power spectra of the observed PNA index (Fig. 3a). The PNA index exhibits statistically significant spectral peaks at the ENSO-dominant interannual frequency band ($f_E \approx 0.2$ –0.4 yr⁻¹), evidence of the direct impact of ENSO on the PNA teleconnection. In addition, the PNA index

also exhibits statistically significant spectral peaks at around 0.6–0.8 yr⁻¹ and 1.2–1.4 yr⁻¹, corresponding to the frequency bands of $1 - f_E$ and $1 + f_E$, respectively. Similar fast near-annual time-scale variability has been found in several previous studies (Stuecker et al. 2013, 2015), which can be explained by the ENSO combination mode (C-mode). The C-mode is found to occur in the Pacific region, arising from the nonlinear atmospheric interaction between the warm-pool SST annual cycle and ENSO SST variability (Stuecker et al. 2013, 2015). It usually enters its peak phase during early spring, approximately 1 to 3 months after ENSO peaks, which strongly affects the northwest Pacific anticyclone and thereby the East Asian monsoon.

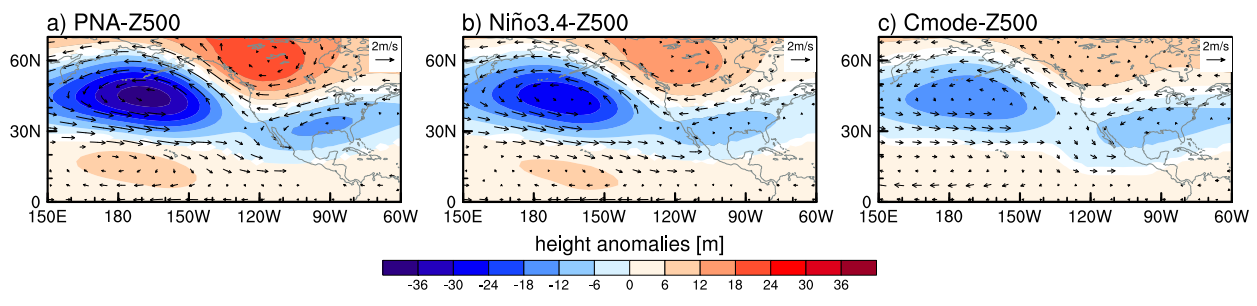


FIG. 6. The 500-hPa geopotential height (shading; m) and horizontal wind (vectors; m s⁻¹) anomalies regressed upon the normalized monthly (a) PNA and (b) Niño-3.4, and (c) C-mode indices for the EXP1. Shaded areas represent anomalies that are statistically significant at the 90% confidence level. The wind anomalies are shown only when they are significant at the 90% confidence level.

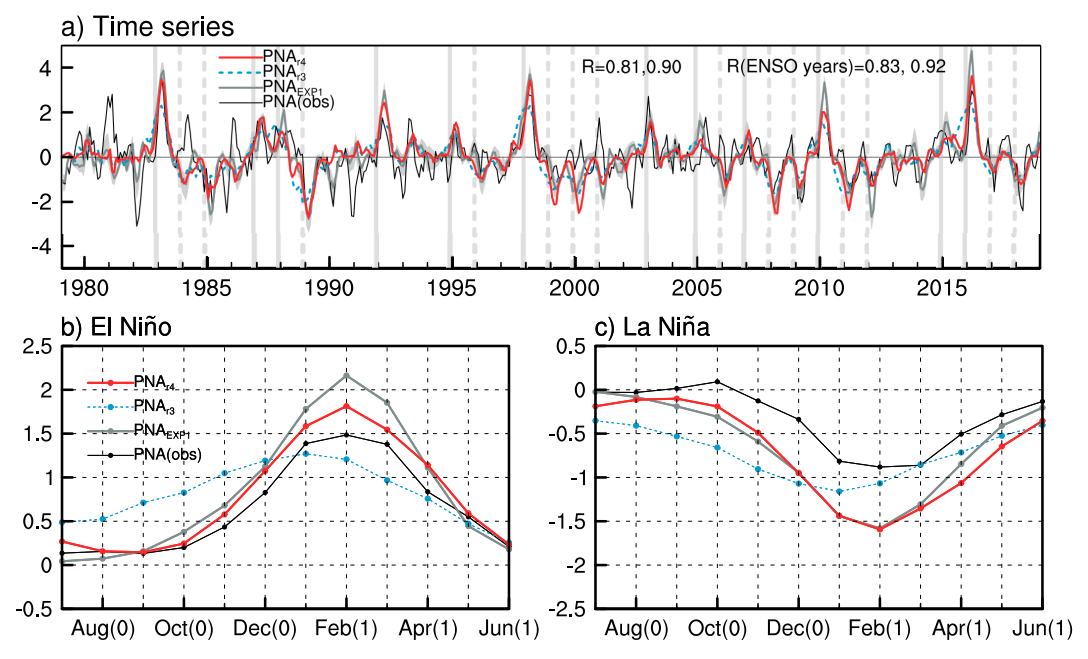


FIG. 7. (a) Time series of the observed PNA index [PNA(obs), black solid line], the simulated PNA_{EXP1} (dark gray solid line), the PNA_{r3} (blue dashed line), and the PNA_{r4} (red solid line). The correlation coefficients of the PNA_{r3} with the observed PNA indices during all years and during ENSO years only are 0.81 and 0.83, respectively. The correlation coefficients of the PNA_{r4} with the observed PNA indices during all years and during ENSO years only are 0.90 and 0.92, respectively. The light gray shading represents the ensemble spread. The gray solid and dashed vertical gray lines correspond to El Niño and La Niña years, respectively. Composite monthly evolution of the PNA(obs) (black solid line), PNA_{EXP1} (dark gray line), PNA_{r3} (blue dashed line), and PNA_{r4} (red solid line) for (b) El Niño years and (c) La Niña years. The abscissa indicates 12 months from July of year(0) to June of year(1).

On the basis of the PNA index's spectral characteristics, we hypothesize that the near-annual variance of the PNA pattern is due to the C-mode. To test our hypothesis, we consider the following theoretical approximation for the C-mode based on Stuecker et al. (2013):

$$C-mode(t) = Ni\tilde{n}o3.4(t)\cos(\omega_a t - \varphi), \tag{1}$$

where the annual cycle is represented by $\cos(\omega_a t - \varphi)$ that has its maximum in February and its minimum in August, ω_a denotes the angular frequency of the annual cycle, and φ is its phase. In Fig. 4a, we show the power spectrum for this idealized C-mode index, which exhibits most of its spectral variance at the ENSO-annual cycle difference $(1 - f_E)$ and sum $(1 + f_E)$ tones, consistent with the fast near-annual time-scale variability in the PNA index. We next display regressed atmospheric circulation anomalies at 500 hPa with respect to the defined C-mode index (Fig. 4b). It reveals that the C-mode-associated circulation pattern is almost identical to the PNA spatial pattern (Fig. 1a), with a pattern correlation of 0.91, suggesting that the C-mode dynamics might contribute to the PNA time evolution.

To provide a more comprehensive understanding of the ENSO-annual cycle nonlinear interaction impacts on the PNA pattern variability, we linearly reconstruct the observed PNA index using the Niño-3.4 index alone (PNA $_{\rm r1}$) and using the Niño-3.4 and C-mode indices together (PNA $_{\rm r2}$), as follows:

$$PNA_{r1}(t) = 0.59 \times Nino3.4(t-1)$$
 (2)

$$PNA_{r2}(t) = 0.52 \times Nino3.4(t-1) + 0.48 \times C\text{-mode}(t-1).$$
(3)

Here, a 1-month lag is used to accommodate the delayed time of the atmospheric response over the mid-high latitudes to tropical Pacific heating (Deser et al. 2017; Alexander et al. 2002). The corresponding regression coefficients are derived using the least squares estimation method. As displayed in Fig. 5a, a positive correlation of 0.52 exists between the PNA_{r1} and the observed PNA indices for all years, and a correlation of 0.63 for ENSO years only. The PNA_{r1} index is characterized by a slow temporal evolution, with its magnitude being about half of the observed PNA index. Considering the additional role of the C-mode, the PNA_{r2} has a correlation of 0.59 with the observed PNA index for all years and a correlation of 0.73 for ENSO years only. Despite a limited increase in the correlation coefficients, the temporal evolution structure and amplitude of the observed PNA pattern are much better reproduced by the PNA_{r2} than the PNA_{r1} during ENSO years. This is clearly seen in the composite seasonal evolution of the observed and reconstructed PNA indices for El Niño and La Niña years (Figs. 5b,c). The PNA_{r1} is characterized by a slow evolution from ENSO developing to decaying summers, whereas the PNA_{r2} well captures the abrupt phase transition of the observed PNA index during

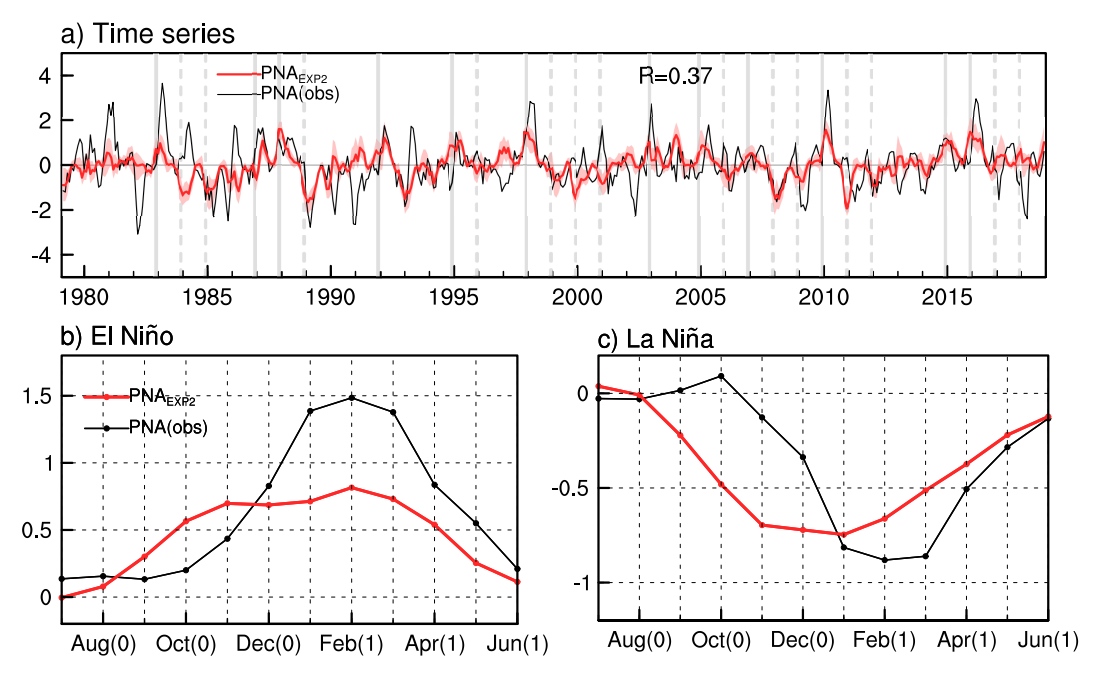


Fig. 8. (a) Time series of the observed PNA index [PNA(obs), black solid line] and the PNA $_{\rm EXP2}$ (red solid line). The correlation coefficient of the PNA $_{\rm exp2}$ with the observed PNA indices during all years is 0.37. The red shading represents the ensemble spread. The gray solid and dashed vertical gray lines correspond to El Niño and La Niña years, respectively. Composite monthly evolution of the PNA(obs) (black solid line) and PNA $_{\rm EXP2}$ (red solid line) for (b) El Niño years and (c) La Niña years. The abscissa indicates 12 months from July of year(0) to June of year(1).

El Niño years and La Niña years. Moreover, the power spectrum of the PNA $_{\rm r2}$ reveals statistically significant peaks at the 90% confidence level in the frequency bands of f_E , $1-f_E$, and $1+f_E$, similar to that shown in the observed PNA index (Fig. 3a). A cross-spectral analysis between the two indices further reveals potential coherence in these frequency bands (Fig. 3b), suggesting that the ENSO–annual cycle nonlinear interaction is a key component of the PNA response to ENSO.

5. PNA seasonal preference and associated mechanisms in numerical experiments

To further support our arguments based on the above observational analyses, we further conduct two sets of sensitivity experiments based on the GFDL AM2.1 atmospheric model (EXP1 and EXP2; see the experimental design in section 2). Figure 6a shows the 500-hPa geopotential height anomalies regressed upon the monthly PNA index in EXP1, which includes the tropical Pacific background SST annual cycle. Here, we use the same definition for the simulated PNA index as for the observations. This atmospheric model well reproduces the observed PNA spatial pattern, with a pattern correlation of 0.93. The simulated PNA index in this experiment shows a statistically significant correlation (R = 0.63, statistically significant at the 99% confidence level) with the observed PNA index during 1979-2019 (Fig. 7a). In particular, the observed sharp phase transition of the PNA pattern during ENSO years is well captured in the EXP1 (Figs. 7b,c).

We also show the simulated extratropical teleconnection patterns corresponding to ENSO and its C-mode variability in the EXP1, highly resembling the PNA pattern over the North Pacific and North America (Figs. 6b,c). As done for the observations, we reconstruct the time series of the PNA_{EXP1} using the Niño-3.4 index alone (PNA_{r3}) and using both the Niño-3.4 and C-mode indices (PNA_{r4}). There is a slight increase in the linear correlation coefficient of the $PNA_{\rm EXP1}$ with the $PNA_{\rm r4}$ compared to that with the PNA_{r3} ($R = 0.81 \rightarrow 0.90$ for all years; $R = 0.83 \rightarrow 0.92$ for ENSO years). Figures 7b and 7c next display the composite time evolution of the observed PNA, PNA_{EXP1}, PNA_{r3}, and PNA_{r4} indices for El Niño and La Niña years, respectively. Consistent with the observed PNA teleconnection pattern, the PNA_{EXP1} exhibits the abrupt phase transition during both El Niño and La Niña events, which cannot be reproduced based on the ENSO SST information alone (PNA_{r3}). Once we additionally consider the ENSO-annual cycle nonlinear interaction, the distinct seasonal synchronization of the simulated PNA pattern in the EXP1 can be well reproduced (Figs. 7b,c). Thus, our model experiments further support our hypothesis that the ENSO-annual cycle nonlinear interaction plays a crucial role in the PNA temporal evolution during ENSO years.

To highlight the importance of the annual cycle to the seasonal preference of PNA teleconnection, we also conduct a sensitivity experiment in which we exclude the annual cycle of the tropical Pacific SST. Relative to the EXP1, the simulated PNA pattern in the EXP2 (PNA $_{\rm EXP2}$) displays a much weaker correlation (R=0.37, statistically significant at

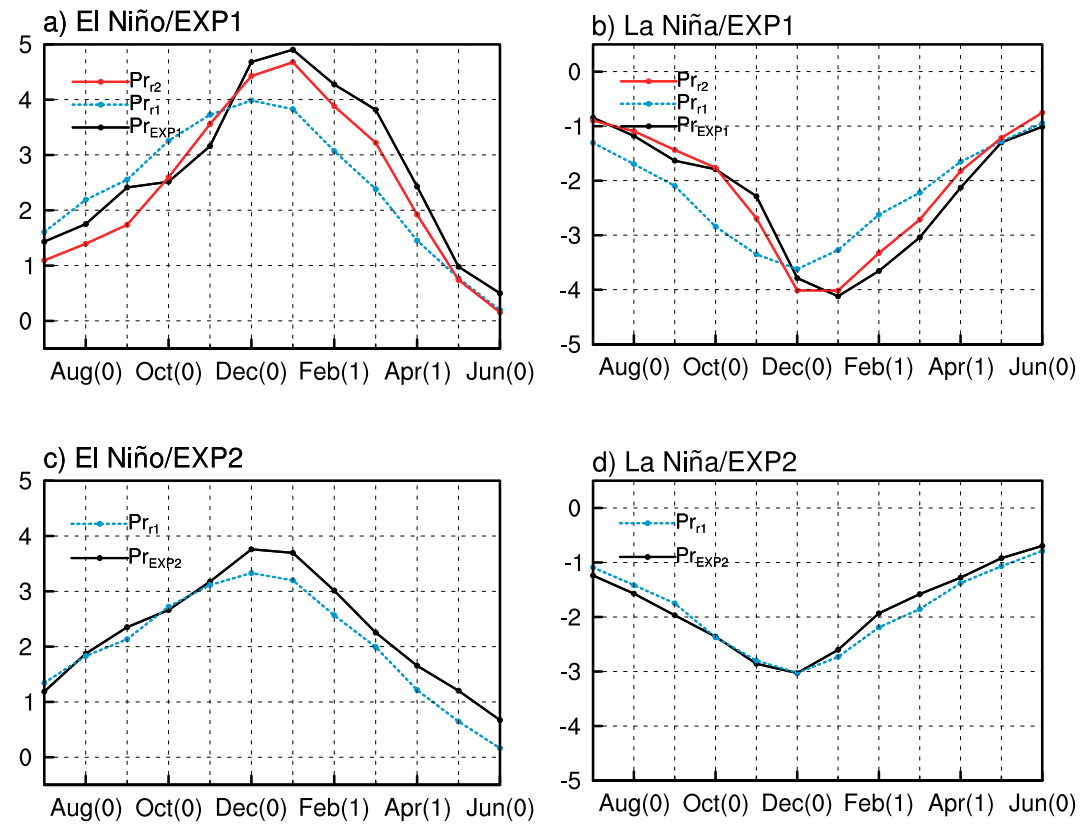


FIG. 9. Composite monthly evolution of the ENSO-associated tropical precipitation anomalies (mm day $^{-1}$) in EXP1 (Pr_{EXP1}; black solid line), the linearly reconstructed Pr_{EXP1} index using only Niño-3.4 index as the independent variable based on regression analysis (Pr_{r1}; blue dashed line), and the linearly reconstructed Pr_{EXP1} index using both the Niño-3.4 and C-mode indices as independent variables based regression analysis (Pr_{r2}; red solid line) for (a) El Niño years and (b) La Niña years. Composite monthly evolution of the ENSO-associated tropical precipitation anomalies (mm day $^{-1}$) in EXP2 (Pr_{EXP2} (black solid line), the linearly reconstructed Pr_{EXP2} index using only Niño-3.4 index as the independent variable based on regression analysis (Pr_{r1}; blue dashed line) for (c) El Niño years, and (d) La Niña years. The corresponding regression coefficients are derived using the least squares estimation method. The abscissa indicates 12 months from July of year(0) to June of year(1).

the 99% confidence level) with the observed PNA index. The PNA_{EXP2} reconstructed with the direct ENSO forcing exhibits a slower temporal evolution and weaker amplitude compared to the PNA_{EXP1}, which includes the effect of the annual cycle modulation. This difference can be more clearly shown in the composite of El Niño and La Niña events (Figs. 8b,c), where EXP2 fails to reproduce the abrupt phase transition of the PNA teleconnection that is seen both in the observations and EXP1. The above results highlight the importance of the tropical Pacific SST annual cycle in causing the seasonally modulated response of the PNA teleconnection pattern to ENSO. These results also provide a plausible explanation for the overestimation of ENSO teleconnection over the North Pacific in models (Chen et al. 2020, 2022). Since our experimental designs for the EXP1 and EXP2 differ only in the background SST, the model bias in simulating the ENSO teleconnection may be related to the model's ability to reproduce the realistic background SST annual cycle over the tropical Pacific and its interaction with ENSO.

One issue that deserves further attention is how the tropical Pacific SST annual cycle exerts impacts on the temporal evolution of the PNA teleconnection during ENSO years. Previous studies demonstrated that the nonlinear interaction of ENSO with the local background SST annual cycle is usually manifested in the ENSO-associated precipitation and lowlevel wind fields (Stuecker et al. 2015, 2013; Fukuda et al. 2021). The related convection then provides a crucial bridge to connect the tropical SST anomalies and extratropical atmospheric teleconnection (e.g., Cai et al. 2014; Chiodi and Harrison 2015, 2013). This can be clearly seen by comparing the tropical central-eastern Pacific convection response in the two experiments with and without consideration of the background SST annual cycle. Based on the composite difference pattern of precipitation anomalies between El Niño and La Niña events (not shown), our focus lies on the analysis of convection anomalies in the region of 10°S-5°N, 150°-210°E, as ENSO-related precipitation anomalies predominantly occur in this area.

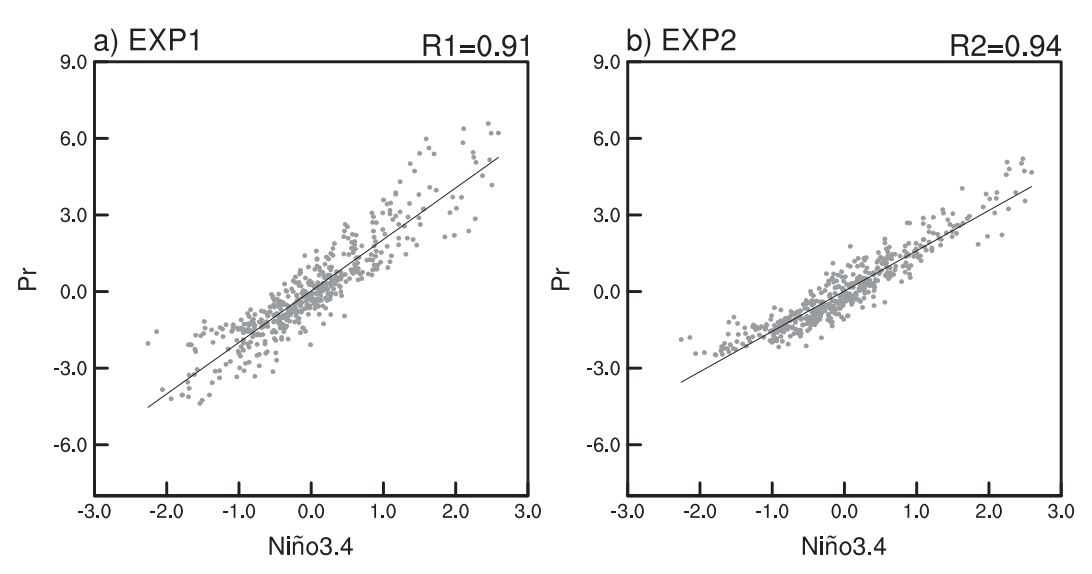


FIG. 10. Scatterplots of monthly tropical Pacific precipitation anomalies against monthly Niño-3.4 SST anomalies in (a) EXP1 and (b) EXP2. The black line denotes the corresponding linear fitting line for all months.

In EXP1, with the SST annual cycle included, the anomalous convection over the central-eastern tropical Pacific exhibits also an abrupt phase transition with rapid enhancement in boreal winter, which is well explained by the combination of the ENSO SST anomalies and the SST annual cycle-ENSO interaction (Figs. 9a,b). In contrast, the background SST annual cycle in the tropical Pacific is not considered in EXP2; hence, the tropical Pacific anomalous convection keeps pace with slow ENSO SST anomaly evolution (Figs. 9c,d). Since the SST annual cycle is not considered in this experiment, the role of nonlinear interaction between the ENSO and the annual cycle is absent and, therefore, the abrupt phase transition of the tropical Pacific convection anomalies cannot be reproduced. Figure 10 further displays the scatterplot of monthly precipitation anomalies and the Niño-3.4 SST index. In both EXP1 and EXP2, a robust correlation exists between monthly precipitation anomalies and ENSO SST anomalies, with correlation coefficients of $R_1 = 0.91$ and $R_2 =$ 0.94, respectively. However, in contrast to that in EXP2, more dots in EXP1 are located far from the linear fitting line, due to the modulation of the background SST annual cycle.

Next, we reconstruct linearly PNA_{EXP1} and PNA_{EXP2} using the anomalous convection over the central-eastern tropical Pacific in EXP1 and EXP2, respectively, based on regression analysis. As displayed in Fig. 11, a positive correlation of 0.85 (statistically significant at the 99% confidence level) is shown between PNA_{EXP1} and its reconstruction, whereas there is a positive correlation of 0.64 (statistically significant at the 99% confidence level) between PNA_{EXP2} and its reconstruction. These significant correlations between the simulated and reconstructed PNA indices during ENSO years both in EXP1 and EXP2 indicate the direct connection between the ENSOassociated anomalous tropical convection and the PNA teleconnection pattern. The slightly weakened correlation in EXP2 is possibly related to our experimental design in which the SST boundary forcing is fixed to September equinox conditions (no annual cycle). The cold tongue is strongest in September, which could lead to a weaker ENSO-associated tropical convection response and, thus, weaker control of ENSO on the extratropical atmospheric teleconnection, compared to EXP1. The above results suggest that suggests that the ENSO-associated

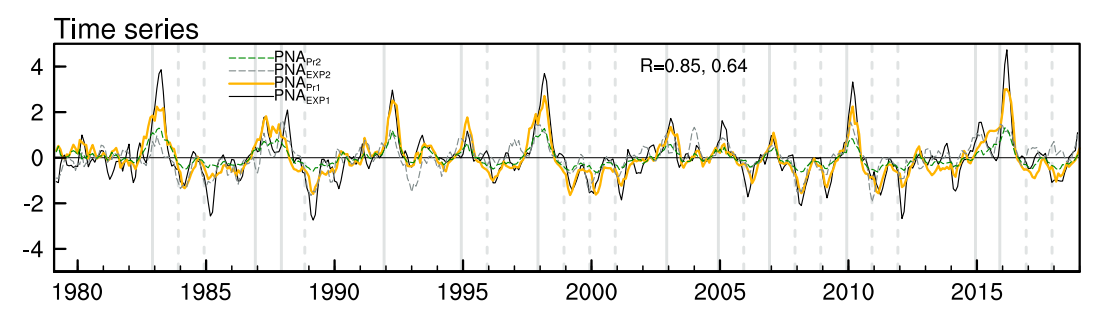


FIG. 11. Time series of the PNA_{EXP1} (black solid line), the PNA_{EXP2} (gray dashed line), and the linearly reconstructed PNA_{EXP1} and PNA_{EXP2} indices using the Pr_{EXP1} and Pr_{EXP2} as the independent variable based on regression analysis, respectively (PNA_{Pr1} , yellow solid line; PNA_{Pr2} , green dashed line). The correlation coefficient of the PNA_{exp1} with the PNA_{Pr1} indices is 0.85. The correlation coefficient of the PNA_{exp2} with the PNA_{Pr2} indices is 0.64.

tropical Pacific convection modulated by the background SST annual cycle is of critical importance in the seasonal synchronization of the PNA teleconnection pattern during ENSO years.

6. Conclusions and discussion

In the present study, we investigated the temporal evolution of the PNA teleconnection during ENSO years using observations along with targeted, atmospheric general circulation model experiments. Different from the relatively slow evolution of the ENSO SST anomalies, the PNA teleconnection pattern exhibits much faster time scales, including its rapid establishment in late winter during ENSO years. The PNA pattern displays statistically significant spectral peaks in the frequency bands of f_E , $1 - f_E$, and $1 + f_E$. The fast near-annual time-scale variability of the PNA pattern is due to ENSO's C-mode originating from nonlinear interactions between ENSO and the annual cycle. The PNA temporal evolution during ENSO years is reproduced well in the atmospheric general circulation model when both ENSO SST anomalies and the SST annual cycle are prescribed as boundary conditions. However, the observed temporal evolution of the PNA teleconnection pattern cannot be reproduced when we exclude the SST annual cycle in the tropical Pacific. We have shown that the background SST annual cycle in the tropical Pacific strongly modulates the ENSO-associated precipitation response, thereby determining the temporal evolution of the PNA teleconnection during ENSO years.

This work investigates the crucial role of ENSO-associated, tropical central Pacific convection in the temporal evolution of the PNA teleconnection pattern, highlighting the effect of the interaction between ENSO and the background SST annual cycle. Recent studies also pointed out the potential impact of anomalous convection over the tropical western Indian Ocean on the ENSO-related PNA pattern seasonality (Park et al. 2023; Abid et al. 2021). These findings underscore the need for further research to understand the possible linkage between convection anomalies in other tropical regions and the C-mode, as well as their role in the teleconnection of ENSO. On the other hand, the seasonal preference of climate phenomena is commonly linked to the seasonally varying basic state (Newman and Sardeshmukh 1998; Branstator and Frederiksen 2003). We here emphasize that the tropical Pacific SST annual cycle plays a crucial role in the seasonal preference of the PNA response to ENSO. Other components of the annual cycle have also been proposed to be of importance (e.g., Branstator 1985; Sardeshmukh and Hoskins 1988; Hoskins and Karoly 1981). For instance, it has been shown that the propagation of atmospheric Rossby waves is modulated by the climatological basic flow in the extratropics. The possible impacts from the basic flow, in particular, the annual cycle of the midlatitude jet stream, need to be considered to fully understand the PNA variability in the future in addition to the tropical Pacific SST annual cycle.

Acknowledgments. This work is inspired by the initial study of Li-Ciao Hong during her postdoctoral visit at the University of Hawaii in 2015. This work is supported by the National

Nature Science Foundation of China (42125501) and the Postgraduate Research and Practice Innovation Program of Jiangsu Province (KYCX22_1132). M.F.S. was supported by NSF Grant AGS-2141728. This is IPRC Publication Number 1604 and SOEST Contribution Number 11691.

Data availability statement. The data that support the findings of this study are available from the NCEP/NCAR Reanalysis 1 webpage (https://psl.noaa.gov/data/gridded/data.ncep. reanalysis.html) and the Met Office Hadley Centre observations datasets (https://www.metoffice.gov.uk/hadobs/hadisst/data/download.html).

REFERENCES

- Abid, M. A., F. Kucharski, F. Molteni, I.-S. Kang, A. M. Tompkins, and M. Almazroui, 2021: Separating the Indian and Pacific Ocean impacts on the Euro-Atlantic response to ENSO and its transition from early to late winter. *J. Climate*, 34, 1531–1548, https://doi.org/10.1175/JCLI-D-20-0075.1.
- Alexander, M. A., I. Bladé, M. Newman, J. R. Lanzante, N.-C. Lau, and J. D. Scott, 2002: The atmospheric bridge: The influence of ENSO teleconnections on air–sea interaction over the global oceans. *J. Climate*, **15**, 2205–2231, https://doi.org/10.1175/1520-0442(2002)015<2205:TABTIO>2.0.CO;2.
- Anderson, J. L., and Coauthors, 2004: The new GFDL global atmosphere and land model AM2-LM2: Evaluation with prescribed SST simulations. *J. Climate*, 17, 4641–4673, https://doi.org/10.1175/JCLI-3223.1.
- Bladé, I., M. Newman, M. A. Alexander, and J. D. Scott, 2008: The late fall extratropical response to ENSO: Sensitivity to coupling and convection in the tropical west Pacific. *J. Cli-mate*, 21, 6101–6118, https://doi.org/10.1175/2008JCLI1612.1.
- Branstator, G., 1985: Analysis of general circulation model sea-surface temperature anomaly simulations using a linear model. Part II: Eigenanalysis. J. Atmos. Sci., 42, 2242–2254, https://doi.org/10.1175/1520-0469(1985)042<2242:AOGCMS>2. 0.CO:2.
- —, and J. Frederiksen, 2003: The seasonal cycle of interannual variability and the dynamical imprint of the seasonally varying mean state. J. Atmos. Sci., 60, 1577–1592, https://doi.org/10.1175/3002.1.
- Cai, W., and Coauthors, 2014: Increasing frequency of extreme El Niño events due to greenhouse warming. *Nat. Climate Change*, 4, 111–116, https://doi.org/10.1038/nclimate2100.
- Chen, R., I. R. Simpson, C. Deser, and B. Wang, 2020: Model biases in the simulation of the springtime North Pacific ENSO teleconnection. *J. Climate*, 33, 9985–10002, https://doi. org/10.1175/JCLI-D-19-1004.1.
- —, —, —, and Y. Du, 2022: Mechanisms behind the springtime North Pacific ENSO teleconnection bias in climate models. *J. Climate*, **35**, 7691–7710, https://doi.org/10.1175/JCLI-D-22-0304.1.
- Chiodi, A. M., and D. E. Harrison, 2013: El Niño impacts on seasonal U.S. atmospheric circulation, temperature, and precipitation anomalies: The OLR-event perspective. *J. Climate*, 26, 822–837, https://doi.org/10.1175/JCLI-D-12-00097.1.
- —, and —, 2015: Global seasonal precipitation anomalies robustly associated with El Niño and La Niña events—An OLR perspective. *J. Climate*, 28, 6133–6159, https://doi.org/10.1175/JCLI-D-14-00387.1.

- Davis, R. E., 1976: Predictability of sea surface temperature and sea level pressure anomalies over the North Pacific Ocean. *J. Phys. Oceanogr.*, **6**, 249–266, https://doi.org/10.1175/1520-0485(1976)006<0249:POSSTA>2.0.CO;2.
- Deser, C., I. R. Simpson, K. A. McKinnon, and A. S. Phillips, 2017: The Northern Hemisphere extratropical atmospheric circulation response to ENSO: How well do we know it and how do we evaluate models accordingly? *J. Climate*, 30, 5059–5082, https://doi.org/10.1175/JCLI-D-16-0844.1.
- Feldstein, S. B., 2000: The timescale, power spectra, and climate noise properties of teleconnection patterns. *J. Climate*, **13**, 4430–4440, https://doi.org/10.1175/1520-0442(2000)013<4430: TTPSAC>2.0.CO;2.
- Fukuda, Y., M. Watanabe, and F. Jin, 2021: Mode of precipitation variability generated by coupling of ENSO with seasonal cycle in the tropical Pacific. *Geophys. Res. Lett.*, 48, e2021GL095204, https://doi.org/10.1029/2021GL095204.
- Horel, J. D., and J. M. Wallace, 1981: Planetary-scale atmospheric phenomena associated with the Southern Oscillation. *Mon. Wea. Rev.*, 109, 813–829, https://doi.org/10.1175/1520-0493(1981) 109<0813:PSAPAW>2.0.CO;2.
- Hoskins, B. J., and D. J. Karoly, 1981: The steady linear response of a spherical atmosphere to thermal and orographic forcing. *J. Atmos. Sci.*, 38, 1179–1196, https://doi.org/10.1175/1520-0469(1981)038<1179:TSLROA>2.0.CO;2.
- Jong, B.-T., M. Ting, and R. Seager, 2016: El Niño's impact on California precipitation: Seasonality, regionality, and El Niño intensity. *Environ. Res. Lett.*, 11, 054021, https://doi.org/10. 1088/1748-9326/11/5/054021.
- Kalnay, E., and Coauthors, 1996: The NCEP/NCAR 40-Year Reanalysis Project. *Bull. Amer. Meteor. Soc.*, 77, 437–472, https://doi.org/10.1175/1520-0477(1996)077<0437:TNYRP>2. 0.CO;2.
- Kim, S., H.-Y. Son, and J.-S. Kug, 2018: Relative roles of equatorial central Pacific and western North Pacific precipitation anomalies in ENSO teleconnection over the North Pacific. *Climate Dyn.*, 51, 4345–4355, https://doi.org/10.1007/s00382-017-3779-6.
- Leathers, D. J., and M. A. Palecki, 1992: The Pacific/North American teleconnection pattern and United States climate. Part II: Temporal characteristics and index specification. *J. Climate*, 5, 707–716, https://doi.org/10.1175/1520-0442(1992)005<0707: TPATPA>2.0.CO;2.
- ——, B. Yarnal, and M. A. Palecki, 1991: The Pacific/North American teleconnection pattern and United States climate. Part I: Regional temperature and precipitation associations. *J. Climate*, 4, 517–528, https://doi.org/10.1175/1520-0442(1991) 004<0517:TPATPA>2.0.CO:2.
- L'Heureux, M. L., A. Kumar, G. D. Bell, M. S. Halpert, and R. W. Higgins, 2008: Role of the Pacific-North American (PNA) pattern in the 2007 Arctic sea ice decline. *Geophys. Res. Lett.*, 35, L20701, https://doi.org/10.1029/2008GL035205.
- Li, X., Z.-Z. Hu, P. Liang, and J. Zhu, 2019: Contrastive influence of ENSO and PNA on variability and predictability of North American winter precipitation. *J. Climate*, 32, 6271–6284, https://doi.org/10.1175/JCLI-D-19-0033.1.
- Liu, Z., K. Yoshimura, N. H. Buenning, and X. He, 2014: Solar cycle modulation of the Pacific–North American teleconnection influence on North American winter climate. *Environ. Res. Lett.*, 9, 024004, https://doi.org/10.1088/1748-9326/9/2/024004.
- —, —, Z. Jian, and L. Zhao, 2017: The response of winter Pacific North American pattern to strong volcanic eruptions. *Climate Dyn.*, **48**, 3599–3614, https://doi.org/10.1007/s00382-016-3287-0.

- Livezey, R. E., M. Masutani, A. Leetmaa, H. Rui, M. Ji, and A. Kumar, 1997: Teleconnective response of the Pacific–North American region atmosphere to large central equatorial Pacific SST anomalies. *J. Climate*, 10, 1787–1820, https://doi.org/10.1175/1520-0442(1997)010<1787:TROTPN>2.0.CO:2.
- Montroy, D. L., 1997: Linear relation of central and eastern North American precipitation to tropical Pacific sea surface temperature anomalies. *J. Climate*, **10**, 541–558, https://doi.org/10. 1175/1520-0442(1997)010<0541:LROCAE>2.0.CO;2.
- —, M. B. Richman, and P. J. Lamb, 1998: Observed nonlinearities of monthly teleconnections between tropical Pacific sea surface temperature anomalies and central and eastern North American precipitation. *J. Climate*, 11, 1812–1835, https://doi.org/10.1175/1520-0442(1998)011<1812:ONOMTB>2.0.CO;2.
- Mori, M., and M. Watanabe, 2008: The growth and triggering mechanisms of the PNA: A MJO-PNA coherence. *J. Meteor.* Soc. Japan, 86, 213–236, https://doi.org/10.2151/jmsj.86.213.
- Newman, M., and P. D. Sardeshmukh, 1998: The impact of the annual cycle on the North Pacific/North American response to remote low-frequency forcing. *J. Atmos. Sci.*, 55, 1336–1353, https://doi.org/10.1175/1520-0469(1998)055<1336: TIOTAC>2.0.CO;2.
- O'Reilly, C. H., 2018: Interdecadal variability of the ENSO teleconnection to the wintertime North Pacific. *Climate Dyn.*, 51, 3333–3350, https://doi.org/10.1007/s00382-018-4081-y.
- Park, C.-H., J. Choi, S.-W. Son, D. Kim, S.-W. Yeh, and J.-S. Kug, 2023: Sub-seasonal variability of ENSO teleconnections in western North America and its prediction skill. *J. Geophys. Res. Atmos.*, 128, e2022JD037985, https://doi.org/10.1029/2022JD037985.
- Rayner, N. A., D. E. Parker, E. B. Horton, C. K. Folland, L. V. Alexander, D. P. Rowell, E. C. Kent, and A. Kaplan, 2003: Global analyses of sea surface temperature, sea ice, and night marine air temperature since the late nineteenth century. J. Geophys. Res., 108, 4407, https://doi.org/10.1029/2002JD002670.
- Riddle, E. E., M. B. Stoner, N. C. Johnson, M. L. L'Heureux, D. C. Collins, and S. B. Feldstein, 2013: The impact of the MJO on clusters of wintertime circulation anomalies over the North American region. *Climate Dyn.*, 40, 1749–1766, https:// doi.org/10.1007/s00382-012-1493-y.
- Sardeshmukh, P. D., and B. J. Hoskins, 1988: The generation of global rotational flow by steady idealized tropical divergence. *J. Atmos. Sci.*, 45, 1228–1251, https://doi.org/10.1175/1520-0469(1988)045<1228:TGOGRF>2.0.CO;2.
- Soulard, N., H. Lin, and B. Yu, 2019: The changing relationship between ENSO and its extratropical response patterns. *Sci. Rep.*, **9**, 6507, https://doi.org/10.1038/s41598-019-42922-3.
- Stuecker, M. F., A. Timmermann, F.-F. Jin, S. McGregor, and H.-L. Ren, 2013: A combination mode of the annual cycle and the El Niño/Southern Oscillation. *Nat. Geosci.*, 6, 540– 544, https://doi.org/10.1038/ngeo1826.
- —, F.-F. Jin, A. Timmermann, and S. McGregor, 2015: Combination mode dynamics of the anomalous northwest Pacific anticyclone. *J. Climate*, 28, 1093–1111, https://doi.org/10.1175/JCLI-D-14-00225.1.
- Thomson, D. J., 1982: Spectrum estimation and harmonic analysis. *Proc. IEEE*, **70**, 1055–1096, https://doi.org/10.1109/PROC.1982. 12433.
- Trenberth, K. E., G. W. Branstator, D. Karoly, A. Kumar, N.-C. Lau, and C. Ropelewski, 1998: Progress during TOGA in understanding and modeling global teleconnections associated

- with tropical sea surface temperatures. *J. Geophys. Res.*, **103**, 14291–14324, https://doi.org/10.1029/97JC01444.
- Wallace, J. M., and D. S. Gutzler, 1981: Teleconnections in the geopotential height field during the Northern Hemisphere winter. *Mon. Wea. Rev.*, **109**, 784–812, https://doi.org/10.1175/1520-0493(1981)109<0784:TITGHF>2.0.CO;2.
- Wang, H., and R. Fu, 2000: Winter monthly mean atmospheric anomalies over the North Pacific and North America associated with El Niño SSTs. *J. Climate*, **13**, 3435–3447, https://doi.org/10.1175/1520-0442(2000)013<3435:WMMAAO>2.0.CO;2.
- Webster, P. J., 1981: Mechanisms determining the atmospheric response to sea surface temperature anomalies. *J. Atmos. Sci.*, **38**, 554–571, https://doi.org/10.1175/1520-0469(1981)038<0554: MDTART>2.0.CO;2.
- Yeh, S.-W., and Coauthors, 2018: ENSO atmospheric teleconnections and their response to greenhouse gas forcing. Rev. Geophys., 56, 185–206, https://doi.org/10.1002/2017RG000568.
- Younas, W., and Y. Tang, 2013: PNA predictability at various time scales. *J. Climate*, **26**, 9090–9114, https://doi.org/10.1175/ JCLI-D-12-00609.1.